STEADY, PERIODIC, QUASI-PERIODIC AND CHAOTIC FLOW REGIMES IN TOROIDAL PIPES

Michele Ciofalo[*+]; Massimiliano Di Liberto [*], Ivan Di Piazza[**]

[*]*Dipartimento dell'Energia, Università di Palermo, Viale delle Scienze, 90128 Palermo, Italy*
[**]*ENEA UTIS-TCI, C.R. Brasimone, 40032 Camugnano(Bo), Italy*
[+]Corresponding author; email ciofalo@din.unipa.it

ABSTRACT

Incompressible flow in a toroidal pipe was investigated by direct numerical simulation [1]. The curvature δ=*a*/*c* (radius of the cross section / radius of the torus) was 0.3 or 0.1 and the bulk Reynolds number ranged between ~3500 and ~14 700. The study revealed a rich scenario of transition to turbulence.

For the higher curvature δ = 0.3, a supercritical transition from stationary to periodic flow (Hopf bifurcation) was observed at Re≈4600. The periodic flow was characterized by a travelling wave which, in the whole periodic Re range, took the form of a varicose modulation of the twin Dean vortex rings, included 8 wavelengths along the axis of the torus, and exhibited instantaneous anti-symmetry about the equatorial midplane. A further transition to quasi-periodic flow, characterized by two independent fundamental frequencies and their first few harmonics, occurred at Re≈5200. The two frequencies were associated with two travelling wave systems, the first consisting of a varicose modulation of the Dean vortex rings, the second of an array of oblique near-wall vortices produced at the edge of the Dean cells, co-rotating with these latter and travelling from the inner towards the outer side, against the secondary circulation.

For the lower curvature δ=0.1, the results suggested the existence of a *sub*critical Hopf bifurcation at Re≈5200 and of a secondary Hopf bifurcation to quasi-periodic flow at a lower Reynolds number of ~4900. Starting from zero-velocity initial conditions, the steady-state flow remained stable up to a Reynolds number of 5139, while a further increase in Re to 5208 yielded an abrupt transition to quasi-periodic flow which remained stable up to Re=6280 or larger. When a quasi-periodic solution (e.g., that obtained for Re=5658) was used as the initial condition and Re was made to *decrease*, the quasi-periodic regime remained stable down to values of Re well below the subcritical Hopf bifurcation at ~5200. Only a further, substantial decrease of Re to ~4108 led to the smooth disappearance of mode II and to a stable periodic solution. An abrupt transition to stationary flow was obtained when the Reynolds number decreased well below 4000 (e.g., a test case was computed for Re =3490). All periodic and quasi-periodic solutions for δ=0.1 exhibited instantaneous symmetry about the equatorial midplane.

Also the further transition from quasi-periodic to chaotic flow occurred with different mechanisms for the two curvatures. For δ=0.3, quasi-periodic flow was obtained in the whole Reynolds number range 5270-7850. As Re increased slightly beyond this value (Re=8160), strong fluctuations, associated with random streamwise vortices, arose in the outer region. The ensuing chaotic flow regime was characterized by a broadband, almost continuous, frequency spectrum. A further increase of Re to 13180 did not modify to any appreciable extent the flow regime and the distribution of the velocity fluctuation intensity. For δ=0.1, the convergence of the results to quasi-periodic flow became impossible to achieve as Re increased beyond ~6280, and was replaced by long and erratic transients. For Re=8160, the solution, albeit stationary in a statistical sense, was chaotic and exhibited a large number of frequencies, but the outer region remained basically stationary. Only when Re increased further, the outer region became unsteady and was characterized by the production of streamwise vortices which were then transported by the secondary flow destroying all remains of regular oscillations.

1 INTRODUCTION

1.1. *Secondary flow in curved pipes*

Flow in curved pipes is characterized by the existence of a secondary circulation in the cross section, caused by the imbalance between inertial and centrifugal forces. According to Isachenko *et al*. [2], the secondary flow appears when the Reynolds number exceeds $\sim 11.6/\sqrt{\delta}$, e.g. ~36.7 for δ=0.1 and ~21.2 for δ=0.3.

Boussinesq [3] identified the mechanisms driving the secondary flow in a curved duct and predicted the presence of two symmetric secondary vortices. Dean [4], under the hypotheses of small curvature and stationary flow, derived a solution for the stream function of the secondary motion and for the main streamwise velocity. Dean's solution exhibits a shift of the streamwise velocity maximum towards the outer wall and two symmetric recirculation cells (Dean vortices) having a characteristic velocity scale:

$$\hat{u}_{sec} \approx \hat{u}_{av}\sqrt{\delta} \tag{1}$$

in which $\hat{u}_{av}$ is the average streamwise velocity, δ is the non-dimensional curvature *a/c*, *a* is the radius of the section and *c* is the radius of curvature (here and in the following, dimensional quantities will be indicated by a caret ^ while no caret will be used for dimensionless quantities).

The bulk Reynolds number Re is defined as

$$\mathrm{Re} = \hat{u}_{av}\, 2a/\nu \tag{2}$$

while the Dean number is defined as

$$\mathrm{De} = \mathrm{Re}\sqrt{\delta} \tag{3}$$

and takes account of inertial, centrifugal and viscous effects. For small values of the curvature, De becomes the single governing parameter; for example, in terms of the Dean number the above mentioned criterion for the appearance of

secondary flow becomes De>~11.6. A thorough literature review for flow in curved pipes has been presented by Berger *et al.* [5].

1.2. *Transition to turbulence in curved pipes*

Most of the first attempts to determine the conditions for transition to turbulence in curved and helical pipes focussed on the behaviour of global quantities such as the friction coefficient. The earlier departure from the linear pressure drop - flow rate behaviour observed in curved pipes with respect to straight pipes was interpreted in these studies as an indication of an earlier transition to turbulence. However, after the work of Dean [4] and the experiments of Taylor [6], it became clear that the departure from linearity in the pressure drop-flow rate relationship is simply an indication that the flow in curved pipes is not self similar, rather than an indication of departure from laminar flow conditions. Most of the increased resistance in curved pipes is due to the secondary circulation, and a stationary laminar flow is actually maintained in curved pipes up to Re well above the critical value for straight pipes. Narasimha & Sreenivasan [7] showed that, in a helically coiled pipe preceded and followed by straight pipe segments, under appropriate conditions turbulent flow may be observed in these latter while the flow remains laminar in the coils.

Isachenko et al. [2] report the following formula to compute the critical Reynolds number for transition to turbulence:

$$\mathrm{Re}_{cr} = 18500 \cdot \delta^{0.28} \qquad (4)$$

which, for example, provides Re_{cr}=7996 for δ=0.05, Re_{cr}=9708 for δ=0.1 and Re_{cr}=13206 for δ=0.3.

Experimental pressure drop results for a wide range of curvatures and Reynolds numbers were presented by Ito [8], who derived the following correlations for the Darcy-Weisbach friction factor f (four times the Fanning coefficient) in the laminar and turbulent ranges:

$$f = \frac{64}{\mathrm{Re}} \cdot \frac{21.5 \cdot \mathrm{De}}{(1.56 + \log_{10} \mathrm{De})^{5.73}} \qquad \text{(laminar flow)} \qquad (5.a)$$

$$f = 0.304 \cdot \mathrm{Re}^{-0.25} + 0.029\sqrt{\delta} \qquad \text{(turbulent flow)} \qquad (5.b)$$

valid for $5 \cdot 10^{-4} \le \delta \le 0.2$.

Although dated, equations (5) have recently been confirmed to an impressive degree by the extensive experimental work of Cioncolini & Santini [9] in a broad range of curvatures ($0.027 \le \delta \le 0.143$) and Reynolds numbers ($\mathrm{Re} \approx 10^3$-$7 \cdot 10^4$). For relatively high values of the curvature ($0.0416 \le \delta \le 0.143$), the friction coefficient decreases monotonically with Re and transition to turbulence is indicated by a change in slope of the f–Re curve. Therefore, for sufficiently high curvatures, an indicative value of the critical Reynolds number for transition to turbulence can be provided by the intersection of fully laminar and fully turbulent asymptotic laws. An approximate correlation which expresses this criterion for the critical Reynolds number is:

$$\mathrm{Re}_{cr} = 2100 \cdot \left(1 + 15\delta^{0.57}\right) \qquad (6)$$

which, for example, provides Re_{cr}=7811 for δ=0.05, Re_{cr}=10578 for δ=0.1 and Re_{cr}=17958 for δ=0.3 (which, however, is beyond its range of validity).

For lower curvatures (δ<0.0416), Cioncolini and Santini [9] observed that, in the proximity of transition, the f-Re curves exhibited a local minimum followed by an inflection point and by a local maximum. Under such circumstances, different transition criteria may be specified on the basis of some feature of the f curves, but may not coincide with the actual onset of turbulence.

Also alternative transition correlations proposed by Ito [8], Srinivasan *et al.* [10] and other authors are based on different interpretations of the f(Re) behaviour for different δ, but do not really capture the specific dynamics of the transition process. All the proposed criteria, however, agree that the effect of curvature is to increase Re_{cr} with respect to straight pipes.

Few studies have investigated transition in curved pipes by direct measurement of local flow quantities. Sreenivasan & Strykowski [11] obtained experimental results in helically coiled pipes with a curvature ratio δ=0.058 and a negligible torsion. Hot-wire velocity measurements were taken after 5 helix turns where the flow was fully developed, and the Reynolds number range investigated varied from 4200 to 6730. For Re=4200 the hot wires registered flat signals corresponding to a laminar stationary flow. For Re=5000, a periodically oscillating behaviour was observed in the inner region and a small-amplitude, high-frequency intermittent oscillation in the outer region. For Re=5870, a not perfectly periodic behaviour was observed in the inner region, and a substantial intermittent turbulent oscillation in the outer region. For Re=6730, the behaviour was fully turbulent both in the inner and in the outer region. The outer side appeared to be the critical region for transition to a chaotic behaviour, since both intermittency and high frequencies first appeared there.

Webster & Humphrey [12] investigated flow in helical coils by LDV for Re≈3800-10500 and $\delta \approx 5.5 \cdot 10^{-2}$. For Reynolds numbers between 5060 and 6330 (De=1190-1480) the authors described a periodic flow characterized by a dimensionless frequency f≈0.14 (normalized by the reference frequency $\hat{u}_{av}/a$). They attributed the origin of this periodic flow to an instability of the outward-directed midplane jet. Transition to turbulence proper was observed only for Re≥6330. In later work [13] the same authors performed flow visualization by dye streaks for the same curvature and Reynolds number range. On the basis of these new results, they identified the cause for flow periodicity in a travelling-wave instability of the Dean vortices of the varicose type, i.e., one in which the axis of each vortex ring remains approximately a circumference, while the vortex intensity varies periodically streamwise (as opposed to a *sinuous* instability, which would involve a periodic lateral oscillation of the vortex ring axes). For Re=5060, they estimated the wavelength to be $(2\pi c)/20$ and the wave phase speed (celerity) to be ~$0.825\,\hat{u}_{av}$; these values changed little with Re. Also the experimental results of Sreenivasan and Strykowski [11] for similar values of the curvature ($\delta = 5.8 \cdot 10^{-2}$) and of the Reynolds number (Re≈5000) are compatible with a travelling wave solution located mainly the inner (Dean vortex) region**,** although the authors did not explicitly suggest this interpretation (previous reports of travelling wave phenomena deserve a special attention since the present paper is largely devoted to the analysis of such structures).

1.3. *Computational studies*

Following two-dimensional perturbation studies [14-16], which assumed the flow to be axially fully developed and thus are of limited interest here, the first three-dimensional

numerical simulations of incompressible turbulent flow in helical and curved pipes were presented by Friedrich and co-workers [17]. They compared toroidal and helical pipe results for Re≈5600 (Re_τ≈230) and δ=0.1. Although the authors performed a statistical processing of the computational results (e.g. by computing Reynolds stress distributions in the cross section), the case they studied was not actually turbulent, but rather a time-dependent laminar flow, as indicated by the experimental results obtained under similar conditions by Webster & Humphrey [13] and Sreenivasan & Strykowski [11] and by the results of the present study (see below). It must also be observed that in the simulations by Hüttl & Friedrich [17] only a small portion of pipe, 7.5 diameters long, was modelled, using periodic boundary conditions at the ends; such simulations would be inadequate to predict travelling waves.

Also Webster & Humphrey [13] complemented their experimental investigation by numerical simulations, performed by discretizing the Navier-Stokes equations written in the local toroidal reference frame, i.e. neglecting coil torsion. The length of the computational domain was chosen equal to the experimentally measured wavelength, thus forcing the travelling wave to possess *a-priori* prescribed features. Under conditions in which experiments evidenced a travelling wave instability, the numerical results showed oscillating velocities with maximum rms values in the proximity of the Dean vortices. Quantitative comparison with experiments was not possible due to the purely qualitative (flow-visualization) nature of these latter.

Travelling waves in a curved square duct were found both experimentally and numerically by Mees *et al*. [18]. The travelling wave mode developed from the stationary four-cell flow typical of curved square ducts, and was characterized by the oscillation of the outer vortices.

2 MODELS AND METHODS

2.1. *Computational domain, governing equations, boundary and initial conditions*

Figure 1(a) shows a schematic representation of the toroidal computational domain; the major radius will be indicated with *c*, the minor radius with *a*. The inner side will be indicated with *I* and the outer side with *O*; here and in all the subsequent figures showing cross sections of the pipe, the *O* side will be on the right and the *I* side on the left, and the view will be along the flow direction, i.e. looking from upstream. The azimuthal angle θ will be measured in the clockwise direction, with $\theta(I)=-\pi/2$, $\theta(O)=\pi/2$.

The continuity and Navier-Stokes equations for a constant-property fluid were solved in the Cartesian orthogonal reference frame $\hat{x}_j=(\hat{x},\hat{y},\hat{z})$ of figure 1. In dimensional form:

$$\frac{\partial \hat{u}_j}{\partial \hat{x}_j}=0 \tag{7}$$

$$\frac{\partial \hat{u}_i}{\partial \hat{t}}+\frac{\partial \hat{u}_i\hat{u}_j}{\partial \hat{x}_j}=-\frac{1}{\rho}\frac{\partial \hat{p}}{\partial \hat{x}_i}+\frac{\partial}{\partial \hat{x}_j}\nu\frac{\partial \hat{u}_i}{\partial \hat{x}_j}+\frac{p_{s,i}}{\rho} \tag{8}$$

Here, p_s is a driving force per unit volume directed along the axis of the pipe which balances frictional losses, so that $p_{s,1}=-p_s\sin\Theta$, $p_{s,2}=p_s\cos\Theta$, $p_{s,3}=0$, Θ being the azimuth around the torus' axis *z*, see figure 1. This is equivalent to imposing the equilibrium mean shear stress $\hat{\tau}_0=(a/2)p_s$, with corresponding friction velocity $\hat{u}_\tau=\sqrt{\hat{\tau}_0/\rho}$, and thus the friction Reynolds number $\mathrm{Re}_\tau=\hat{u}_\tau a/\nu$.

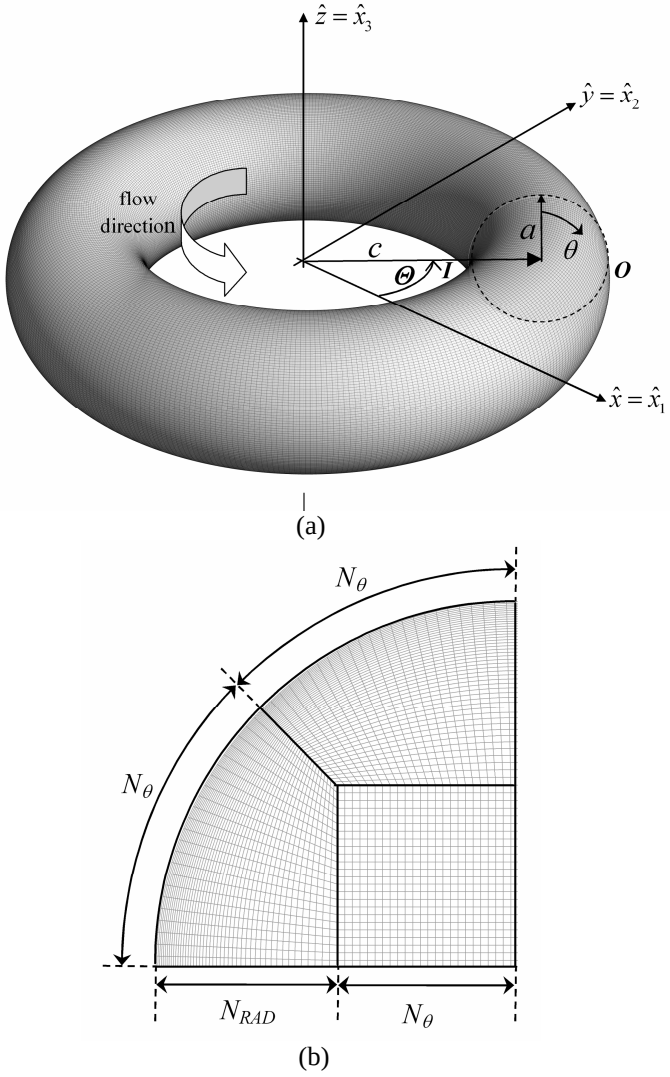

Figure 1. (a) Toroidal pipe (computational domain): *a*, tube radius; *c*, coil radius. (*I*), (*O*) denote inner and outer sides; θ is the azimuth in the cross-section, measured clockwise with $\theta(I)=-\pi/2$, $\theta(O)=\pi/2$; Θ is the angular displacement of the cross section from the *x*-*z* plane. (b) One fourth of the cross section of the multi-block structured mesh. The total number of cells in the whole cross section is $N_{SEC}=4N_\theta(N_\theta+2\,N_{RAD})$.

Although the simulations were conducted in a Cartesian orthogonal reference frame, for post-processing and discussion purposes a cylindrical reference frame $(\hat{r}_p,\Theta,\hat{z})$ was used for the whole torus, $\hat{r}_p$ being the normal distance from the torus' axis *z*; the direction Θ of the main flow is also indicated by *s* (for "streamwise") in the figures. A local 2-D polar reference frame $(\hat{r},\theta)$ was also used in the plane of the generic cross section, so that the secondary flow in this plane may be alternatively represented by its components u_r, u_θ along $(\hat{r},\theta)$ or by its components u_{rp}, u_z along $(\hat{r}_p,\hat{z})$.

No slip conditions were imposed at the wall. Zero velocity initial conditions were set for most of the numerical simulations; instabilities, if any, were triggered by small numerical fluctuations due to truncation and round-off errors. A few cases were restarted from a solution obtained for a higher Reynolds number, as discussed in Section 5.

2.2. *Scales*

Although the friction velocity $\hat{u}_\tau = \sqrt{(a/2)\,p_s/\rho}$ is the *a-priori* known quantity, the average velocity $\hat{u}_{av}$ was chosen as a more natural velocity scale. The corresponding frequency scale is:

$$\hat{f}_0 = \frac{\hat{u}_{av}}{a} = \frac{\mathrm{Re}}{2}\cdot\frac{\nu}{a^2} \qquad (9)$$

proportional, by the factor Re/2, to the molecular momentum diffusion frequency ν/a^2. The time scale follows as $\hat{t}_0 = 1/\hat{f}_0$. The "natural" scale for angular velocity is $\hat{\omega}_0 = 2\pi\hat{f}_0$. The wall shear stress was scaled by $\rho\hat{u}_{av}^2$.

All coordinates were scaled by the cross section radius a; thus, the non-dimensional local radial coordinate, measured from the centre of the cross section, is $r = \hat{r}/a$ while the non-dimensional distance from the torus' axis z is $r_p = \hat{r}_p/a$.

2.3. *Numerical method and computational mesh*

The computational method was based on a finite-volume coupled algebraic multigrid solver, and adopted the central interpolation scheme for the advection terms and a second-order backward Euler time stepping algorithm. The computational domain was partitioned into equally-sized blocks which were assigned to different processes, generally running in parallel on 16 cores.

The mesh was multi-block structured, and was characterized by the parameters N_{RAD} and N_θ as shown in figure 1(b). The values used in the present work were N_{RAD}=46, N_θ=24; grid refinement was applied near the wall, with a maximum/minimum cell size ratio of ~5 in the radial direction. With these choices, the cross section was resolved by 11136 cells. In the streamwise direction the domain was discretized by N_{AX} =1024 cells for δ=0.1 and N_{AX}=300 cells for δ=0.3; this led to an overall number of cells of 11.4×10^6 for δ =0.1 and 3.34×10^6 for δ=0.3. The surface mesh for the case δ=0.3 is visible in figure 1(a).

The time step was set equal to $0.8(\nu/u_\tau^2)$ for all cases; this time discretization was judged adequate to capture the dynamic features of the time-dependent flows on which this study is focussed. For the present streamwise grid, this choice led to a Courant number slightly less than 1.

3 FLOW REGIME TRANSITIONS

A systematic investigation was carried out for each curvature by letting the friction Reynolds number Re_τ vary from 232 to 519 (δ=0.3) or from 164 to 476 (δ=0.1). The corresponding bulk Reynolds number varied between 4515 and 13180 for δ=0.3 and between 3490 and 14700 for δ=0.1. For both curvatures, steady state flow was predicted for $\mathrm{Re}\le\mathrm{Re}_c$ and time dependent flow for $\mathrm{Re}>\mathrm{Re}_c$, Re_c being a critical Reynolds number which was estimated to be ~4575 for δ=0.3 and ~5175 for δ=0.1. However, the transition scenario was different for the two curvatures as discussed below.

For the higher curvature δ=0.3, a full sequence of flow regimes from stationary (S) to periodic (P), quasi-periodic (QP) and chaotic (C) flow was observed, similar to that reported for Taylor-Couette flow between concentric cylinders [19] and coherent with the classic Ruelle-Takens route to turbulence. This is illustrated in figure 2(a) by reporting the root mean square value u_s^{rms} of the oscillatory component of the streamwise velocity in a point of a generic cross section located at r=0.8, θ=-π/4 (i.e., within the upper Dean vortex) against the difference between the Reynolds number Re and the critical Reynolds number Re_c. The results suggest the existence of a supercritical Hopf bifurcation from stationary to periodic flow at $\mathrm{Re}=\mathrm{Re}_c$ (point H in the figure), followed by a secondary Hopf bifurcation from periodic to quasi-periodic flow at $\mathrm{Re}\approx\mathrm{Re}_c$+500 (Re≈5075, point H2 in the figure). Symbols denote computational predictions; different shapes are used for S, P and QP solutions. Both the H and the H2 transitions were of the "soft" type, i.e., a generic flow quantity like u_s^{rms} varied continuously as Re crossed the relevant bifurcation value. As discussed in detail in Sections 5.1 and 5.2, the transition from S to P flow was accompanied by a breaking of the instantaneous symmetry with respect to the torus midplane; the ensuing anti-symmetry was preserved also in the QP flow regime. Transition to turbulence (not illustrated in figure 2(a) for scale reasons) occurred only at Re≈8000 (~Re_c+3500).

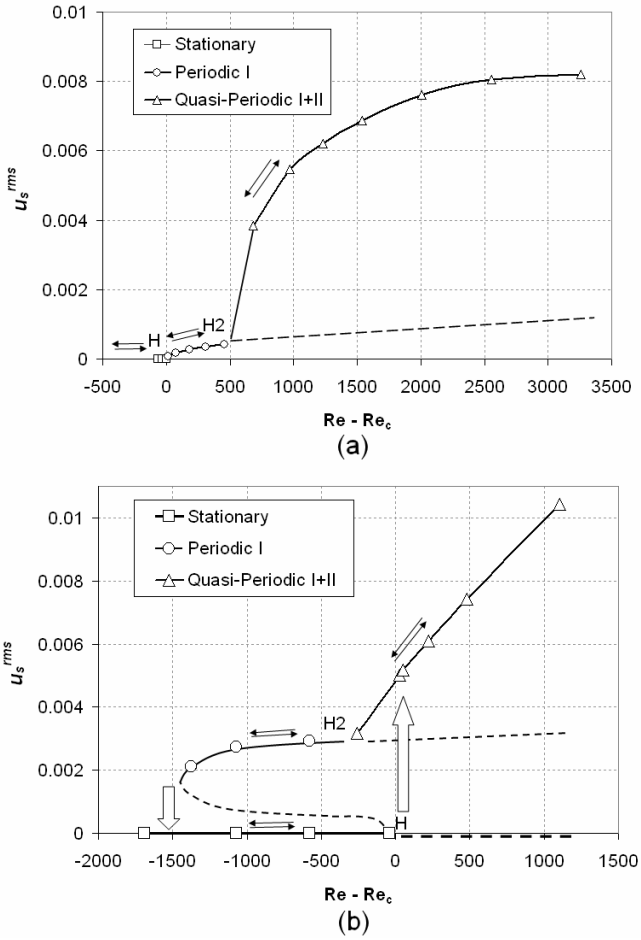

Figure 2. Bifurcation diagrams for δ=0.3 (a) and δ=0.1 (b). The abscissa is the difference between the Reynolds number Re and the Reynolds number Re_c of the Hopf bifurcation; the ordinate is the rms value of the oscillatory component of the streamwise velocity in a generic cross section for r=0.8, θ=$-\pi$/4. H=Hopf bifurcation; H2=secondary Hopf bifurcation; solid lines: stable branches; broken lines: unstable branches.

For the lower curvature δ=0.1, a more complex sequence of flow regimes was observed. This is illustrated in figure 2(b), which reports the same quantity u_s^{rms} as in figure 2(a). In simulations starting either from zero velocity or from the

immediately lowest-Re solution, an abrupt ("hard") transition from S to QP flow occurred when the Reynolds number exceeded $Re_c \approx 5175$. The QP regime was maintained up to a Reynolds number of ~8000 as for $\delta=0.3$. However, simulations conducted by starting from a QP case and reducing the Reynolds number *below* Re_c led to a QP solution for Re=4920 ($Re-Re_c \approx -255$) and to P solutions for Re=4600, 4108 and 3800 ($Re-Re_c \approx -575, -1067$ and -1375, respectively). Only a further reduction to Re=3490 ($Re-Re_c \approx -1685$) led to steady-state flow. Thus, the results exhibited *hysteresis*: some solutions could be obtained only by approaching them backward from higher-Reynolds numbers, and in a certain range of Re multiple solutions (S–P or even S–QP) were obtained for the same Reynolds number depending on the path followed. Interestingly, unlike case $\delta=0.3$, all the P and QP solutions exhibited instantaneous symmetry with respect to the torus midplane. The bifurcation diagram sketched in figure 2(b) is compatible with all the results obtained. It includes a subcritical Hopf bifurcation (H) at $Re=Re_c$ (~5175), an unstable periodic branch, a turning point between Re≈3500 and Re≈4000, a stable periodic branch and a secondary Hopf bifurcation (H2) at Re≈4900. To the best of the authors' knowledge, a comparable transition scenario has not been reported previously in the literature for other flows. Transition to turbulence is not illustrated in figure 2(b) for scale reasons.

Table 1 summarizes the eight selected test cases presented in detail in this paper. They cover the two values of the curvature $\delta=0.3$ and $\delta=0.1$, denoted by D3 and D1, and all four different regimes S, P, QP and C. Both Reynolds numbers Re and Re_τ are provided in Table 1 along with the Dean number De. The friction factor can be computed as $f=32(Re_\tau/Re)^2$ and its values predicted by Ito's resistance correlations (4) are also reported for comparison purposes; however, it should be observed that neither of equations (4) is strictly applicable to the cases with $\delta=0.3$.

Table 1 Main test cases simulated. Flow regimes are indicated by S (stationary), P (periodic), QP (quasi-periodic), C (chaotic).

Case	D1-S	D1-P*	D1-QP	D1-C
δ	0.1	0.1	0.1	0.1
Re_τ	217	184	232	305
Re	5139	4108	5658	8160
De	1625	1299	1789	2561
Regime	S	P	QP	C
$f(\times 10^2)$	5.718	6.400	5.391	4.484
$f(\times 10^2)$ lam, eq.(5a)	5.627	6.331	5.352	4.445
$f(\times 10^2)$ turb, eq.(5b)	n.a.	n.a.	n.a.	4.117

* attained only by letting Re decrease from case D1-QP

Case	D3-S	D3-P	D3-QP	D3-C
δ	0.3	0.3	0.3	0.3
Re_τ	234	247	290	361
Re	4556	4899	6128	8160
De	2495	2732	3356	4475
Regime	S	P	QP	C
$f(\times 10^2)$	8.449	8.119	7.190	6.256
$f(\times 10^2)$ lam, eq.(5a)	7.825	7.546	6.756	5.879
$f(\times 10^2)$ turb, eq.(5.b)	n.a.	n.a.	n.a.	4.786

4 STATIONARY FLOW

Stationary flow was obtained for Re=4515 and 4556 ($\delta=0.3$) and for Re=3490, 4108, 4600 and 5139 ($\delta=0.1$). The two test cases D3-S ($\delta=0.3$, Re=4556) and D1-S ($\delta=0.1$, Re=5139) were chosen as representative. The corresponding values of Re_τ, De and other global quantities are reported in table 1. The higher values of the friction coefficient f obtained for D3-S with respect to D1-S are justified by the higher Dean number, and thus by the more intense secondary circulation associated with higher curvatures. Note that, since stationary solutions are strictly two-dimensional, a fully three-dimensional simulation would not have been necessary in these cases, but this can be stated only *a posteriori*.

Selected results for these two cases are reported in figure 3. Graphs (*a*, *c*) in the left column report contours of the streamwise velocity u_s. Graphs (*b*, *d*) in the right column report vector plots of the secondary motion in their top half, with the reference vector corresponding to $\hat{u}_{av}$ drawn, and corresponding streamlines in the bottom half. The solution is always symmetric with respect to the equatorial midplane of the torus.

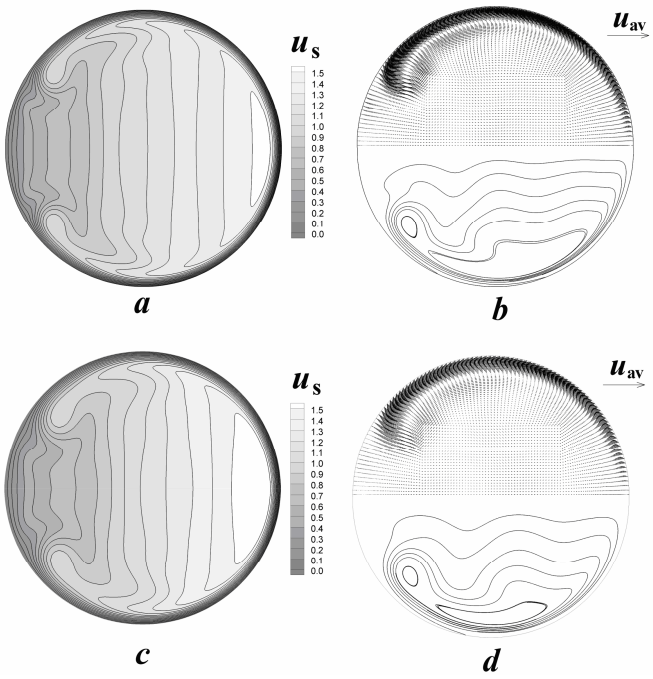

Figure 3. Dimensionless solutions for the stationary cases D3-S (top row) and D1-S (bottom row): (*a*), (*c*) contours of the streamwise velocity; (*b*), (*d*) secondary flow vector plot (reference vector drawn besides) in the upper half and streamlines in the lower half of the section.

Figure 3 shows that the streamwise velocity maximum is shifted towards the outer (*O*) wall and that a roughly linear stratification of the streamwise velocity along the *I-O* direction exists in the core region. The shape and extent of the inner-wall vortices is typical of high-De flow and is coherent with computational results obtained by other authors. In each of the twin vortices the streamlines are winding and strongly asymmetric with respect to the vertical midline of the section and exhibit two separate maxima, i.e. two closed-circulation regions; by contrast, in low-De flows the streamlines are almost elliptic in shape and are roughly symmetric with respect to the vertical midline of the cross section [20]. Only small differences exist between the two curvatures.

5 UNSTEADY LAMINAR FLOW

5.1 *Case D3-P (δ=0.3, Re=4899)*

For δ=0.3 periodic flow was obtained for Reynolds numbers of 4605, 4660, 4768, 4899 and 5042. In particular, detailed results will be illustrated for case D3-P (δ=0.3, Re=4899).

Figure 4(*a*) reports time samples of the streamwise velocity fluctuations u_s–$\langle u_s \rangle$ at two arbitrary points of the cross section, located one in the upper secondary flow boundary layer and one in the upper Dean vortex region, over a dimensionless time interval of 30 starting from an arbitrary instant. The periodicity is clearly visible at both locations; oscillations are small (~0.6%) in the Dean vortex region and even smaller (~0.03%) in the secondary flow boundary layer region. Frequency spectra of the same two quantities, taken over a dimensionless time interval of ~140, are reported in figure 4(*b*). The signals relative to both monitoring locations exhibit a sharp peak at a dimensionless frequency f^{I}≈0.238; harmonics at f=2f^{I} and 3f^{I} are present in the Dean vortex region but negligible in the secondary flow boundary layer.

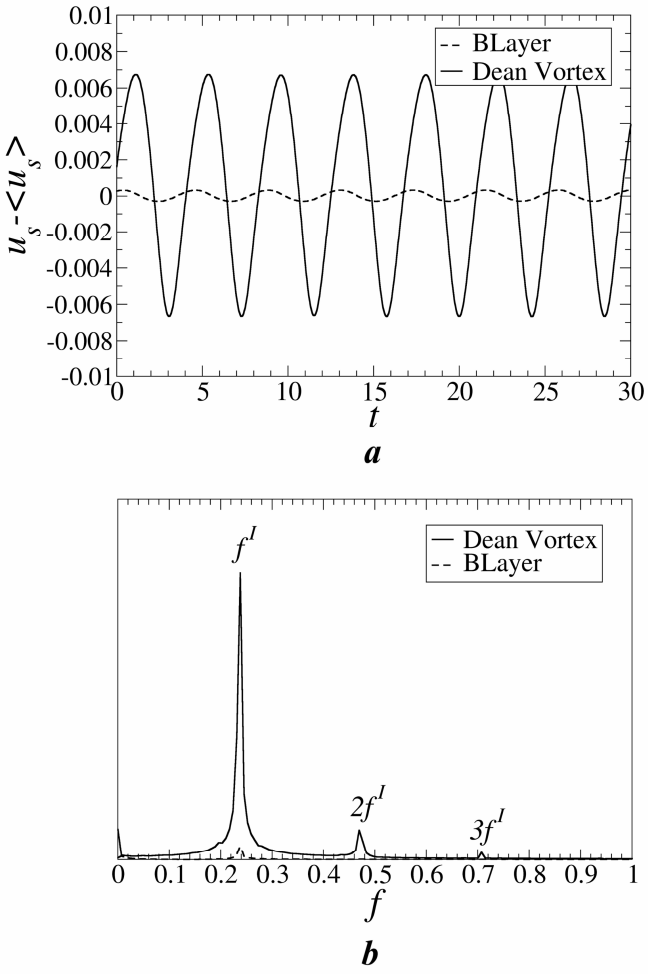

Figure 4. Test case D3-P (Re=4899, δ=0.3): (*a*) behaviour of the streamwise velocity fluctuations at two points of the cross section, located in the Dean vortex region and in the secondary flow boundary, respectively; (*b*) corresponding velocity power spectra (arbitrary units).

The spatial structure of the flow oscillations is more clearly visible in figure 5, which reports the instantaneous distribution of the vertical velocity component u_z on the equatorial midplane. This distribution exhibits k^{I}=8 cells and rotates rigidly along the torus as a travelling wave with a linear celerity (evaluated at the mean radius c) of ~0.623 $\hat{u}_{av}$. Note that this is less than the mean fluid velocity, so that the wave lags behind the fluid over most of the toroidal volume.

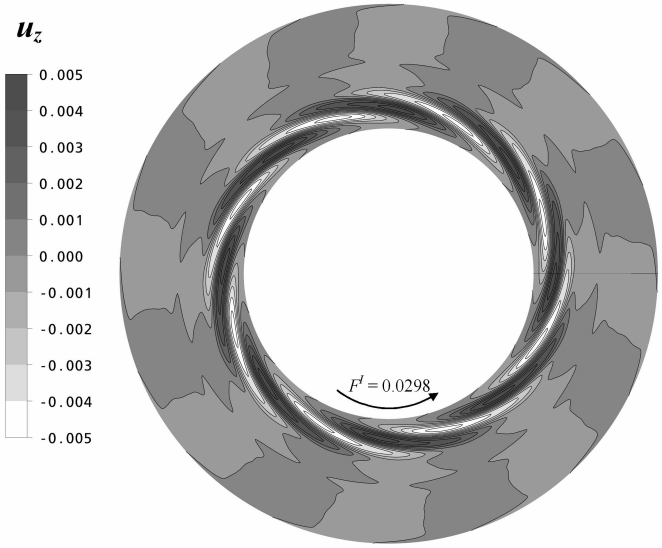

Figure 5. Test case D3-P (Re=4899, δ=0.3): instantaneous distribution of the vertical velocity u_z on the equatorial midplane. Directions and angular celerities of the travelling wave are indicated.

All the periodic cases simulated for δ=0.3 (ranging from Re=4605 through Re=5042) exhibited the same wavelength number k^{I}=8. Also the dimensionless modal frequency remained about constant (~0.238) in this range.

5.2 *Case D3-QP (δ=0.3, Re=6128)*

For δ=0.3 quasi-periodic flow was obtained for Reynolds numbers of 5270, 5562, 5819, 6128, 6594, 7142 and 7850. In particular, detailed results will be illustrated in figures 6-8 for case D3-QP (δ=0.3, Re=6128).

Figure 6(*a*) reports time samples of the streamwise velocity fluctuations u_s-$\langle u_s \rangle$ at two arbitrary points of the cross section, located in the upper secondary flow boundary layer and in the upper Dean vortex region, over a dimensionless time interval of 30 starting from an arbitrary instant. The oscillatory non-periodic unsteadiness is clearly visible. Frequency spectra of the same two quantities, taken over a dimensionless time interval of ~220, are reported in figure 6(*b*). The signals relative to both monitoring locations exhibit sharp peaks at dimensionless frequencies of ~0.400 (f^{I}) and ~0.165 (f^{II}), while secondary harmonics are very small. Within the present frequency resolution limits Δf=1/Δt≈0.005, the two values 0.165 and 0.400 are totally unrelated and thus must be regarded as two incommensurate frequencies characterizing a quasi-periodic flow. Spectra computed for different points of the flow field and different flow quantities exhibited, in all cases, only the independent frequencies f^{I}, f^{II} and their first few harmonics.

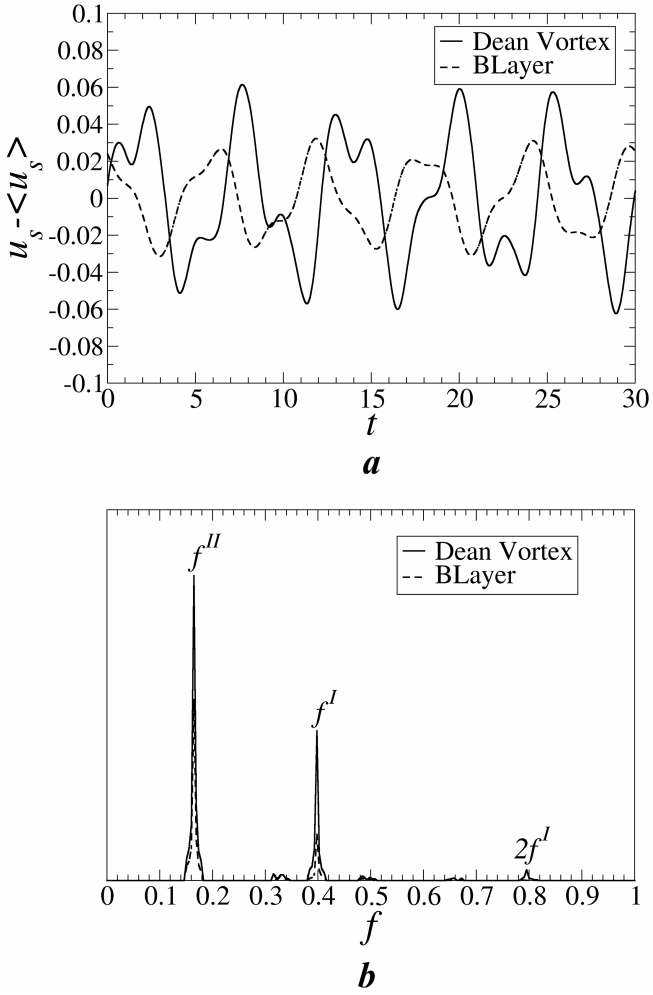

Figure 6. Test case D3-QP (Re=6128, δ=0.3): (*a*) behaviour of the streamwise velocity fluctuations at two points of the cross section, located in the Dean vortex region and in the secondary flow boundary, respectively; (*b*) corresponding velocity power spectra (arbitrary units).

The modal filters G^I and G^{II} sketched in Figure 7 were now used to split the spectral components of the flow associated with mode I and mode II, respectively.

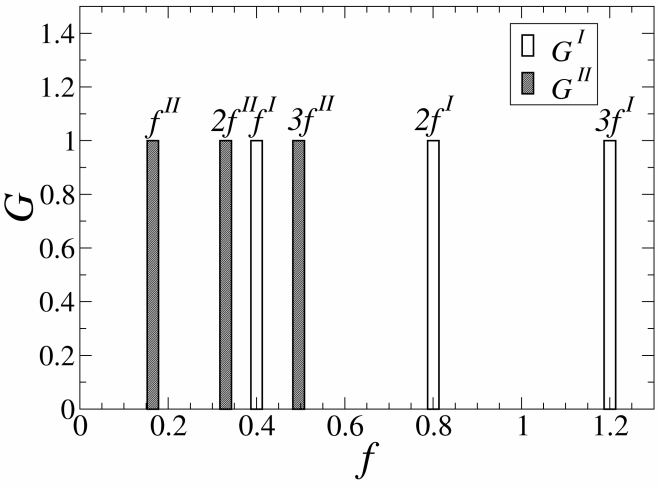

Figure 7. Test case D3-QP (Re=6128, δ=0.3): filter functions G^I and G^{II} used to separate modes I and II.

The spatial structure of mode I is visible in figure 8(*a*), which reports the instantaneous distribution of the vertical velocity component u_z on the equatorial midplane, where the contribution of mode II is small. This distribution exhibits k^I=7 cells and rotates rigidly (or, more exactly, its pure mode I component rotates rigidly) along the torus as a travelling wave with a linear celerity of ~1.19 $\hat{u}_{av}$. This is close to the mean fluid velocity so that the wave leads the fluid in the inner (slow moving) region while it lags behind it in the outer (fast moving) region. It should be observed that the fundamental frequency f^{I} (~0.400) is much larger than the periodic frequency f^{I} of case D3-P (~0.238); therefore, the transition from periodic to quasi-periodic flow, with the appearance of the second fundamental frequency f^{II}, is accompanied by a strong increase of the fundamental frequency associated with the varicose modulation of the Dean vortex ring. Since the number of wavelengths along the torus changes only from 8 to 7, this increase in f^{I} is mainly due to the increase of the linear wave celerity from 0.623 to 1.19 $\hat{u}_{av}$.

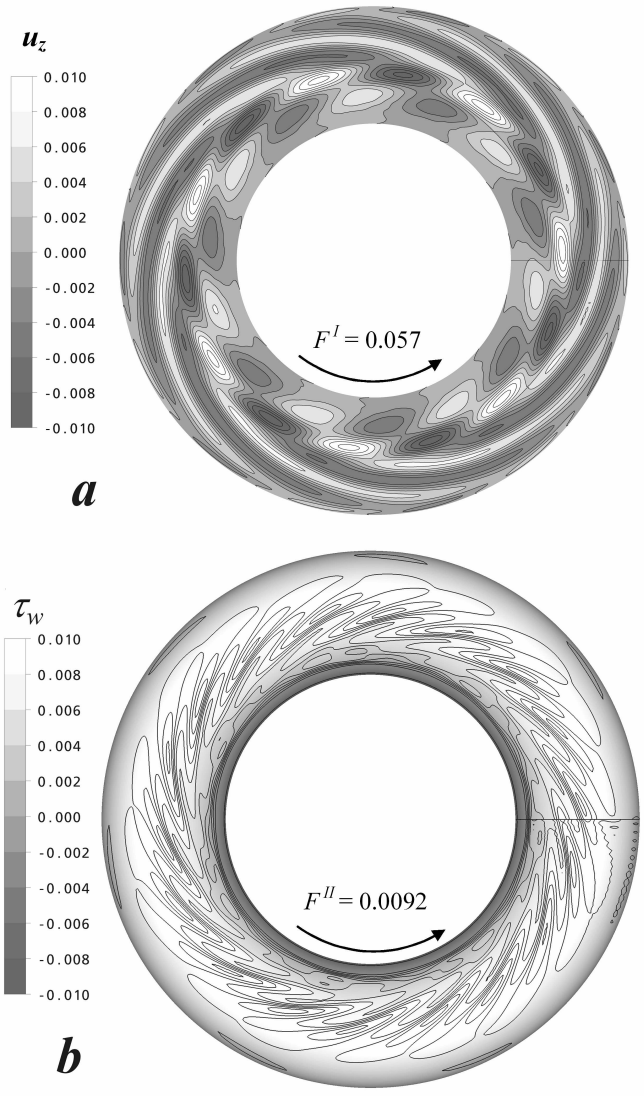

Figure 8. Test case D3-QP (Re=6128, δ=0.3): (*a*) instantaneous distribution of the vertical velocity u_z on the equatorial midplane; (*b*) instantaneous distribution of the wall shear stress on the torus' surface. Directions and angular celerities of travelling waves I and II are indicated.

In the generic cross section, the second mode (mode II) manifests itself in the form of a pair of vortex sheets which occupy the secondary flow boundary layers and move against the mean secondary flow, from the *I* side towards the *O* side.

For this curvature not only mode I, but also mode II (and therefore the whole time-dependent part of the flow field) is anti-symmetric with respect to the equatorial midplane of the torus. The spatial structure of mode II fluctuations is shown in figure 8(*b*), which reports the instantaneous distribution of the wall shear stress module on the surface of the toroidal pipe, where the contribution of mode-I oscillations is small. For the present curvature, the distribution exhibits k^{II}=18 cells and rotates rigidly (or rather, its pure mode II component rotates rigidly) along the torus as a travelling wave having a linear celerity of ~0.19 $\hat{u}_{av}$, much less than the mean fluid velocity and than the linear celerity of mode-I wave.

Summarizing, the unsteady flow exhibited by test case D3-QP can be described as the superposition of two independent systems of travelling waves. Each system consists of a spatially periodic *k*-cell pattern (mode) which rotates rigidly around the torus in the same direction as the mean flow with its own characteristic celerity. Conventionally, we denoted by 'mode I' that mainly concentrated in the Dean vortex region; this mode is the less energetic of the two, consists of a varicose modulation of the Dean vortex rings, and manifests itself in the cross section as a pulsatile motion of the Dean vortices. The second mode, conventionally denoted as 'mode II', is mainly concentrated in the secondary flow boundary layers and is the more energetic of the two. In space, it consists of two arrays of oblique vortices co-rotating with the Dean ones; in the cross section, it manifests itself as a pair of vortex trails generated at the edge of the Dean vortices and moving upstream with respect to the mean secondary flow, from the *I* to the *O* side. The whole fluctuating flow field is instantaneously anti-symmetric with respect to the equatorial midplane of the torus.

In the quasi-periodic range examined (Re=5270-7850) the mode-I wavelength number k^I decreased from 8 (Re=5270) to 7 (Re=5562 and larger), while the dimensionless mode-I frequency f^I increased from 0.275 to 0.400. The mode-II wavelength number k^{II} increased from 10 (Re=5270) to 18 (Re=6128 and larger); the dimensionless mode-II frequency f^{II} increased from 0.035 (Re=5270) to 0.165 (Re=6128) and then decreased slightly for larger Reynolds numbers.

5.3 *Case D1-QP (δ=0.1, Re=5658)*

As anticipated in Section 3, for δ=0.1 an abrupt transition from steady-state to quasi-periodic flow was observed, in simulations starting from zero-velocity conditions or from a lower-Re solution, as soon as the friction Reynolds number exceeded a value of ~218, corresponding to a bulk Reynolds number of ~5175. QP solutions were thus computed for Re=5208, 5236, 5400, 5658 and 6280. Detailed results will be presented here for the test case D1-QP, characterized by δ=0.1, Re=5658.

Figure 9(*a*) reports time samples of the streamwise velocity fluctuations u_s-$\langle u_s \rangle$ at two arbitrary points of the cross section, located in a secondary flow boundary layer and in a Dean vortex region, over a dimensionless time interval of 30 starting from an arbitrary instant. An oscillatory non-periodic unsteadiness is clearly visible. Frequency spectra of the same two quantities, taken over a much longer dimensionless time interval of ~130, are reported in figure 9(*b*). The signal relative to the boundary layer region exhibits a sharp peak at a dimensionless fundamental frequency of ~0.20 (f^{II}) and less marked peaks at the harmonic frequencies $2f^{II}$≈0.40 and $3f^{II}$≈0.60. Shallow peaks are also present at the frequency f^I≈0.27 and its harmonics $2f^I$≈0.54 and $3f^I$≈0.81. The signal relative to the Dean vortex region exhibits its highest peak at the frequency f^I≈0.27, with very shallow secondary peaks at the harmonic frequencies $2f^I$≈0.54, $3f^I$≈0.81; peaks are also present at the frequency f^{II} and its first harmonic $2f^{II}$. Within the present frequency resolution limits Δf=1/Δt≈0.007, the two values 0.20 and 0.27 are totally unrelated and must be regarded as two incommensurate frequencies characterizing a quasi-periodic flow. Spectra for different points of the flow field and different flow quantities exhibited, in all cases, only the two independent frequencies f^I, f^{II} and their first few harmonics.

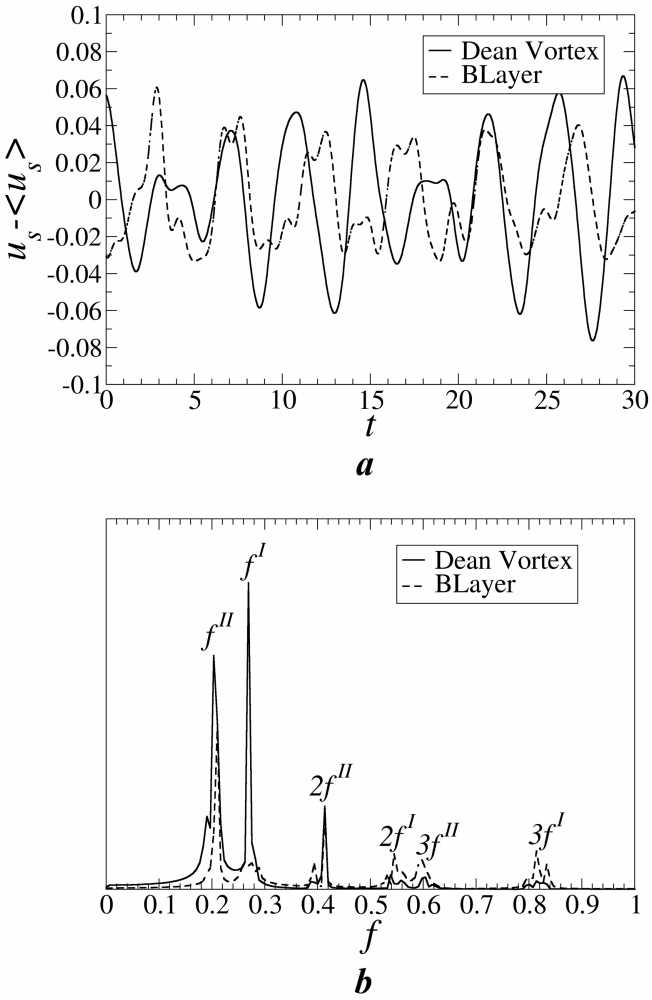

Figure 9. Test case D1-QP (Re=5658, δ=0.1): (*a*) behaviour of the streamwise velocity fluctuations at two points of the cross section, located in the Dean vortex region and in the secondary flow boundary, respectively; (*b*) corresponding velocity power spectra (arbitrary units).

A modal filter similar to that shown in figure 7 was used also in this case to separate mode I and mode II. The spatial structure of mode I is visible in figure 10(*a*), which reports the instantaneous distribution in the equatorial midplane of the secondary flow velocity component u_{rp} directed along the toroidal radius $\hat{r}_p$. Here, the influence of mode II is minor and manifests itself only as a slight departure from exact streamwise periodicity of the pattern shown. This distribution exhibits k^I=16 identical cells; the whole structure (or, more exactly, its pure mode I component) rotates rigidly along the torus as a travelling wave having a linear celerity of ~1.05 $\hat{u}_{av}$. Since this is close to the mean fluid velocity, the wave leads

the fluid in the inner region and lags behind it in the outer region. The above values of k^{I} and of the linear celerity are compatible with those reported by Webster & Humphrey [13] for the lower curvature δ=5.5·10^{-2}.

The spatial structure of mode II is shown in figure 10(*b*), which reports the instantaneous distribution of the wall shear stress module on the surface of the toroidal pipe, where the influence of mode I is marginal. This distribution exhibits k^{II}=36 cells; the whole structure (or, more exactly, its pure mode-II component) rotates rigidly along the torus with a linear celerity of ~0.35 $\hat{u}_{av}$, much less than the mean fluid velocity and than the linear celerity of mode-I wave.

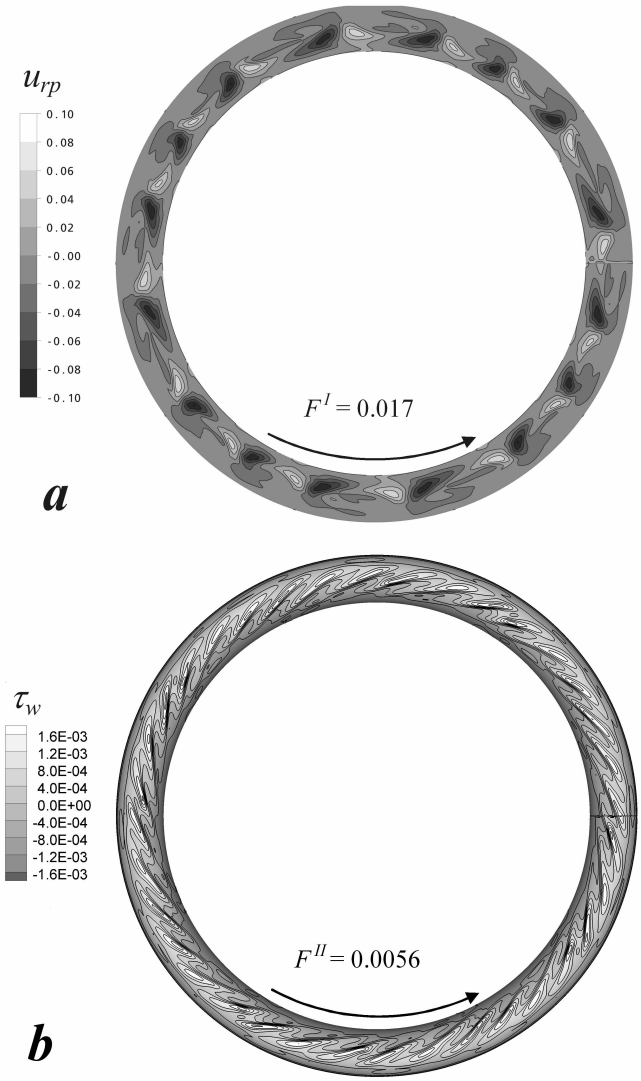

Figure 10. Test case D1-QP (Re=5658, δ=0.1): (*a*) instantaneous distribution of the velocity component along the torus' radius, u_{rp}, in the equatorial midplane; (*b*) instantaneous distribution of the wall shear stress module τ_w on the torus' surface. Directions and angular celerities of travelling waves I and II are indicated.

Summarizing, the unsteady flow exhibited by test case D1-QP can be described, as in case D3-QP, as the superposition of two independent systems of travelling waves; unlike in case D3-QP, the fluctuating flow field is instantaneously symmetric with respect to the equatorial midplane of the torus.

All the quasi-periodic cases simulated for the same curvature δ=0.1, ranging from Re=5208 to 6280, exhibited the same modes and the same number of wavelengths for each mode (k^{I}=16, k^{II}=36). The modal frequencies f^{I} and f^{II} varied only negligibly with Re with respect to the values obtained for the reference case D1-QP (0.27 and 0.20, respectively).

A further QP case was obtained by starting from the solution for case D1-QP (Re=5658) and letting the Reynolds number decrease to ~4920, well below the critical Reynolds number of ~5175 for transition to unsteady flow. This case, unattainable "from below" (i.e., by letting Re increase starting from still fluid or from any lower-Re solution), exhibited the same general features of other quasi-periodic cases, but a reduced number of wavelengths (k^{I}=12) and a larger dimensionless frequency (f^{I}≈0.36) for mode I, while, for mode II, k^{II} and f^{II} were still 36 and 0.20 as in the other QP cases computed for δ=0.1.

As anticipated in Section 3, using the D1-QP solution (Re_τ=232, Re=5658) as initial condition and imposing lower friction Reynolds numbers Re_τ yielded periodic flow (D1-P) at Re=4600, 4108 and 3800 (Re−Re$_c$≈−575, −1067 and −1375, respectively), well below the critical Reynolds number of ~5175 for transition to unsteady flow.

6 CHAOTIC FLOW

The highest Reynolds numbers for which clearly quasi-periodic solutions were obtained were 7859 (δ=0.3) and 6280 (δ=0.1). For the higher curvature (δ=0.3), a moderate increase of Re to 8160 was sufficient to yield a clearly chaotic solution. For δ=0.1, Reynolds numbers in the range ~6500-8000 gave rise to long and erratic transients while clearly chaotic solutions were obtained only for Re>~8000. For both curvatures, results will be presented for a Reynolds number of 8160 (cases D3-C and D1-C).

6.1 *Case* D3-C *(δ=0.3, Re=8160)*

For this case, figure 11(*a*) reports time samples of the streamwise velocity fluctuations u_s-$\langle u_s \rangle$ at two arbitrary points of the cross section, located in the secondary flow boundary layer and in the Dean vortex region. Frequency spectra of the two velocities, taken over a time interval of ~200, are reported in figure 11(*b*). For both locations, spectra exhibit an almost continuous distribution of frequencies, characteristic of highly chaotic flow. Although some peaks stand out on the broad-band background, there is no clear residual of the modal frequencies (f^{I}≈0.4, f^{II}≈0.165) observed in the corresponding quasi-periodic case D3-QP. Similar broad-band spectra are obtained for different points of the flow field and different flow quantities.

For this case, the numerical simulation conducted starting from zero velocity conditions initially yielded a quasi-periodic flow, similar to that predicted for lower Reynolds numbers. However, at a certain instant an instability of the outer region manifested itself in the form of irregular vortices which were rapidly swept by the cross flow into the secondary boundary layers, where they destroyed the regular vortex pattern characteristic of QP flows. Subsequently, the irregularities propagated to the Dean vortex regions until a chaotic flow condition was attained in the whole cross section. These results support the hypothesis that, for this high curvature (δ=0.3), the centrifugal instability of the main flow in the outer region appears to be the mechanism causing the loss of stability of the quasi-periodic solution prevailing at lower Reynolds numbers [1].

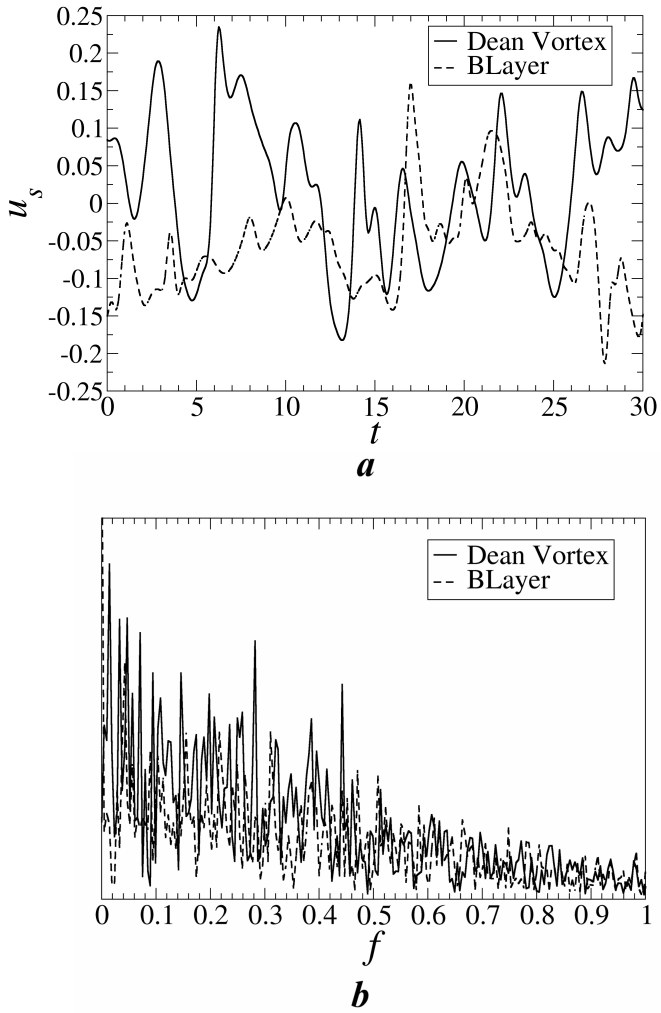

Figure 11. Test case D3-C (Re=8160, δ=0.3): (*a*) behaviour of the streamwise velocity fluctuations at two points of the cross section, located in the Dean vortex region and in the secondary flow boundary, respectively; (*b*) corresponding velocity power spectra (arbitrary units).

The time-averaged secondary flow in the cross section is not illustrated here since, once made dimensionless by the average streamwise velocity, it is almost indistinguishable from that obtained for stationary flow, e.g. case D3-S. This shows that flow unsteadiness, either of regular or chaotic nature, does not significantly affect the time-mean flow: for a given curvature, as the Reynolds number increases, the Dean circulation attains rather early (well within the stationary range) an asymptotic shape and a dimensionless intensity which are little affected (in the average) by the subsequent transitions to unsteady and chaotic behaviour.

A map of the root mean square values of the velocity fluctuations along the streamwise direction for case D3-C is reported in figure 12(a). The outer region has a high level of fluctuations and is the most unsteady. Fluctuations in this region were almost completely absent in the quasi-periodic case D3-QP, and thus appear to be purely chaotic.

A further increase of Re does not change the overall flow structure: figure 12(b) reports the rms streamwise fluctuation for Re=13180, and exhibits no relevant difference with respect to case D3-C in the distribution and dimensionless intensity of turbulence.

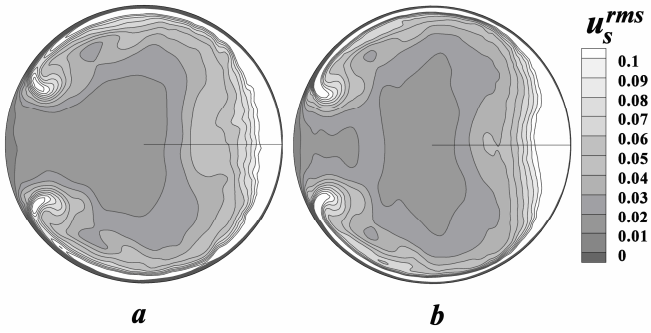

Figure 12. Streamwise root mean square velocity fluctuations for chaotic flow and δ=0.3. (a) Re=8160; (b) Re=13180.

6.2 *Case* D1-C *(δ=0.1, Re=8160)*

For this case, figure 13(*a*) reports time samples of the streamwise velocity fluctuations u_s-$\langle u_s \rangle$ at two arbitrary points of the cross section, located in the secondary flow boundary layer and in the Dean vortex region. The time series in figures 9(a) (case D1-QP) and 13(a) do not show any obvious differences; however, the corresponding power spectra are completely different, see parts (b) of these figures.

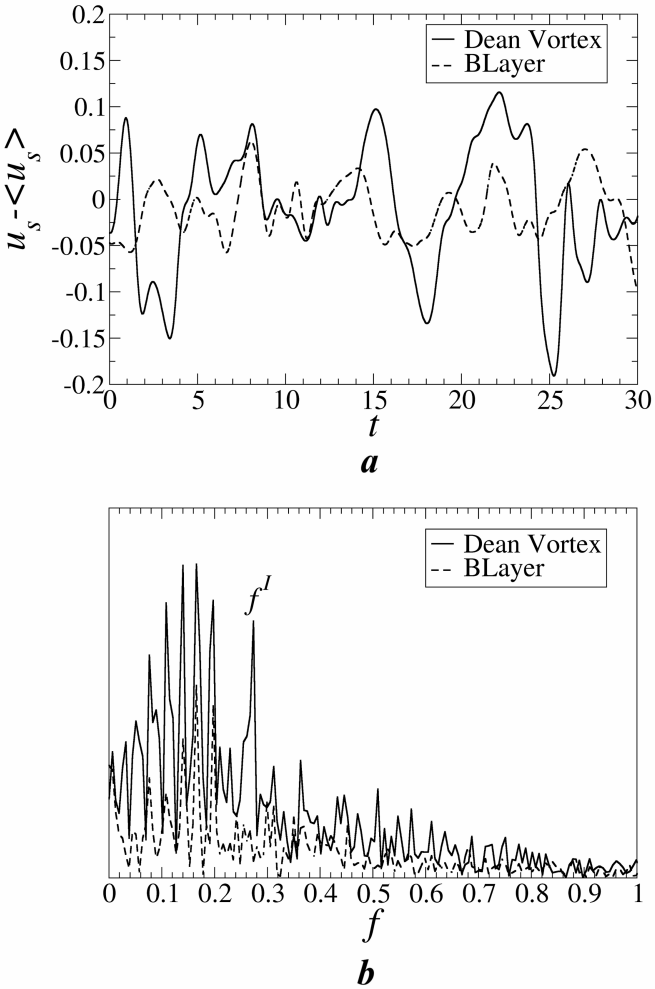

Figure 13. Test case D1-C (Re=8160, δ=0.1): (*a*) behaviour of the streamwise velocity fluctuations at two points of the cross section, located in the Dean vortex region and in the secondary flow boundary, respectively; (*b*) corresponding velocity power spectra (arbitrary units).

For case D1-C, figure 13(b), the spectra for both monitoring points, taken over a dimensionless time interval of ~200, exhibit a large number of peaks occurring at incommensurate frequencies, which is a clear indication of chaotic flow. In the spectrum relative to the Dean vortex, but not in that relative to the boundary layer region, the spectral peak corresponding to the frequency $f^{I}\approx 0.27$ of the mode-I travelling wave (varicose instability of the Dean vortex ring) is still recognizable. The cluster of frequencies observed in the spectra relative to both monitoring points in the interval ~0.1-0.2 replaces the single frequency $f^{II}\approx 0.2$ of mode II (oblique vortex trail in the boundary layer region) and corresponds to a slow, non-sinusoidal, amplitude modulation of the mode-II vortices. Spectra obtained for different points of the flow field and different flow quantities exhibit the same overall chaotic behaviour.The time-averaged secondary flow in the cross section is very similar (once made dimensionless by the average streamwise velocity) to the secondary flow predicted for the stationary case D1-S and is not illustrated here.

A map of the root mean square velocity fluctuation along the streamwise direction for case D1-C is reported in figure 14(a). Of course, fluctuations include all the spectral components, i.e. both chaotic fluctuations proper and what is left of the low-frequency, quasi-periodic oscillations. Figure 14(a) shows that high values of the streamwise fluctuation are attained both in the Dean vortex regions and in the secondary flow boundary layers for $\theta\approx 0$ or π, while the outer region is basically stationary despite the overall chaotic nature of the solution. This suggests that the centrifugal instability of the main flow in this region has not yet manifested itself at the present Reynolds number of 8160.

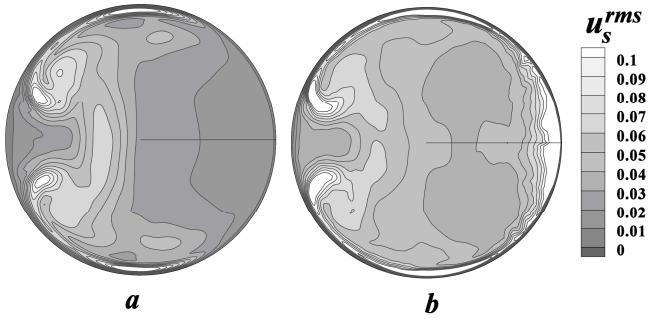

Figure 14. Streamwise root mean square velocity fluctuations for chaotic flow and δ=0.1. (a) Re=8160; (b) Re=14700.

A different picture is obtained if the Reynolds number is further increased: figure 14(b) reports the rms streamwise fluctuation for a higher Re (14700), well into the turbulent range. In this case, fluctuations attain high values not only in the regions mentioned for the lower-Re case, but also near the outer wall, which shows that the centrifugal instability of the main flow in this region has occurred at some Reynolds number intermediate between 8160 and 14700. Since the spatial resolution criteria for the DNS of turbulence are not fully satisfied by the computational mesh for this latter value of Re, the corresponding case will not be analysed in detail here and is reported only for the purpose of comparison with the early-chaotic case D1-C.

7 FLOW REGIME MAP

On the basis of the simulations reported above, of results from the literature, and of asymptotic arguments, a tentative flow regime map in the Re-δ plane can be sketched as in figure 15. This takes into account the present results for δ=0.3 and 0.1, the (qualitative) experimental findings of Sreenivasan & Strykowki [11] for δ=0.058, and the experimental results of Webster & Humphrey [13] for δ=0.055. Here we assumed that the oscillatory flow regimes described by the above authors as periodic are actually instances of quasi-periodic flow. Moreover, the map takes account of the fact that, for δ=0 (straight pipe), a direct transition from stationary laminar to turbulent (chaotic) flow occurs.

The solid lines in figure 15 denote transitions for increasing Re, while the broken lines correspond to transitions for decreasing Re. The regions indicated as P-BW and QP-BW are attainable only by letting the Reynolds number decrease from initial conditions corresponding to a higher-Re solution.

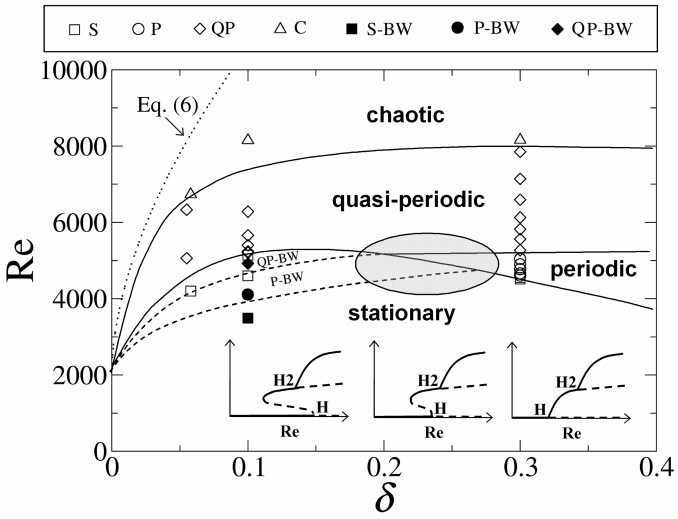

Figure 15. Flow regime map in the Re-δ plane. Symbols: computational or experimental results classified as S (stationary), P (periodic), QP (quasi-periodic) or C (chaotic). S-BW, P-BW and QP-BW denote S, P or QP solutions obtained by letting Re decrease. Solid lines: transitions for increasing Re; broken lines: transitions for decreasing Re. Bifurcation diagrams corresponding to different intervals of δ are drawn in the lower part of the figure. The shaded region is only hypothetical.

Schematic bifurcation diagrams corresponding to different intervals of δ are drawn in the lower part of the figure; in the regions close to δ=0.3 and δ=0.1 they are qualitatively identical to those reported in figures 3(a) and 3(b), respectively. H denotes a Hopf bifurcation from stationary to periodic flow while H2 denotes a secondary Hopf bifurcation from periodic to quasi-periodic flow. The details of the flow regime map in the region of curvatures intermediate between 0.1 and 0.3 are purely hypothetical as suggested by the shaded area. Moreover, a complete regime map would exhibit a finely serrated shape of the transition curves in correspondence with the discrete jump in the number of wavelengths of either mode I or mode II as δ and Re vary, much as in the spiral Poiseuille flow study by Avila *et al*. [21], see e.g. figure 3 therein.

The transition criterion expressed by equation (6) is also reported in figure 15. For any curvature, it predicts a transitional Reynolds number far larger than that associated with transition to chaotic flow on the basis of the present work and of the existing literature. This suggests that transition

correlations like (4) or (6) identify not the onset of turbulence, but rather the attainment of turbulence levels sufficiently high for pressure drop to be dominated by turbulence effects. In fact, in configurations characterized by the presence of secondary flow, pressure drop is largely caused by recirculation and may be significantly higher than in parallel flow also under stationary laminar conditions; the appearance of unsteadiness, and even of turbulence, results in an added frictional term which increases gradually with the Reynolds number and, in low turbulence flows, may represent just a minor contribution to the overall pressure drop.

NOMENCLATURE

a	pipe radius	[m]
c	torus radius	[m]
De	*Dean number*, $\mathrm{Re}\sqrt{\delta}$	
f	Darcy-Weisbach friction coefficient	
f	dimensionless frequency, $\hat{f} / \hat{f}_0$	
$\hat{f}_0$	frequency scale, $\hat{u}_{av} / a$	[s^{-1}]
k	number of wavelengths in the torus	
$\hat{p}$	pressure	[Nm^{-2}]
p_s	driving force per unit volume	[Nm^{-3}]
r	dimensionless radial polar coordinate, $\hat{r} / a$	
$\hat{r}$	radial polar coordinate in cross section	[m]
r_p	dimensionless distance from torus axis, $\hat{r}_p / a$	
$\hat{r}_p$	distance from torus axis	[m]
Re	bulk Reynolds number, $\hat{u}_{av} 2a/\nu$	
Re_τ	friction Reynolds number, $u_\tau a/\nu$	
$\hat{t}_0$	time scale, $a / \hat{u}_{av}$	[s]
$\hat{u}_{av}$	average streamwise velocity	[ms^{-1}]
$\hat{u}_j$	velocity components	[ms^{-1}]
$\hat{u}_{sec}$	scale of secondary velocity	[ms^{-1}]
$\hat{u}_\tau$	equilibrium friction velocity, $\sqrt{\hat{\tau}_0 / \rho}$	[ms^{-1}]
$\hat{x}_j; \hat{x}, \hat{y}, \hat{z}$	Cartesian coordinates	[m]

Greek symbols

δ	curvature, a/c	
Δt	time interval	[s]
θ	azimuthal polar coordinate in cross section	[rads]
Θ	azimuthal angle around torus axis	[rads]
ν	kinematic viscosity	[m^2s^{-1}]
ρ	density	[kg m^{-3}]
$\hat{\tau}_0$	equilibrium mean shear stress, $(a/2)p_s$	[Nm^{-2}]
$\hat{\omega}_0$	angular velocity scale, $2\pi \hat{f}_0$	[rads s^{-1}]

Subscripts, superscripts, averages

cr	critical value for transition
I, O	inner and outer sides of the pipe cross section
RAD, SEC, θ	grid-related subscripts, see figure 1.b
r	along cross section radius
rp	along torus radius
rms	root mean square value of a fluctuation
s	component along pipe axis
I, II	modes of oscillatory flow
0	equilibrium
^	dimensional quantity

REFERENCES

[1] Di Piazza, I. and Ciofalo, M. 2011 Transition to turbulence in toroidal pipes. *J. Fluid Mech.* **687**, 72-117.

[2] Isachenko, V., Osipova, V. and Sukomel, A. 1974 *Heat Transfer*. Second edition, Mir Publishers, Moscow.

[3] Boussinesq, M. J. 1868 Mémoire sur l'influence des frottements dans les mouvements régulier des fluids. *Journal de Mathématiques Pures et Appliquées 2me Série* **13**, 377-424.

[4] Dean, W. R. 1927 Note on the motion of the fluid in a curved pipe. *Phil. Mag.* **4**, 208-223.

[5] Berger, S. A., Talbot, L. and Yao, L. S. 1983 Flow in curved pipes. *Ann. Rev. Fluid Mech.* **15**, 461-512.

[6] Taylor, G. I. 1929 The criterion for turbulence in curved pipes. *Proc. Royal Soc.* **124** (794), 243-249.

[7] Narasimha, R. and Sreenivasan, K. R. 1979 Relaminarization of fluid flows. *Adv. Appl. Mech.* **19**, 221-309.

[8] Ito, H. 1959 Friction factors for turbulent flow in curved pipes. *J. Basic Eng.* **81**, 123-134.

[9] Cioncolini, A. and Santini, L. 2006 An experimental investigation regarding the laminar to turbulent flow transition in helically coiled pipes. *Exp. Thermal Fluid Science* **30**, 367-380.

[10] Srinivasan, S., Nadapurkar, S. and Holland, F. A. 1970 Friction factors for coils. *Trans. Inst. Chem. Eng.* **48**, T 156-T 161.

[11] Sreenivasan, K. R. and Strykowski, P. J. 1983 Stabilization effects in flow through helically coiled pipes. *Exp. Fluids* **1**, 31-36.

[12] Webster, D. R. and Humphrey, J. A. C. 1993 Experimental observations of flow instability in a helical coil. *J. Fluids Eng.* **115**, 436-443.

[13] Webster, D. R. and Humphrey, J. A. C. 1997 Travelling wave instability in helical coil flow. *Phys. Fluids* **9**, 407-418.

[14] Dennis, S. C. R. and Ng, M. 1982 Dual solution for steady laminar flow through a curved tube. *Q. J Mech. Appl. Math.* **35**, 305-324.

[15] Daskopoulos, P. and Lenhoff, A. M. 1989 Flow in curved ducts: bifurcation structure for stationary ducts. *J. Fluid Mech.* **203**, 125-148.

[16] Wang, L. and Yang, T. 2004 Bifurcation and stability of forced convection in curved ducts of square cross-section. *Int. J. Heat Mass Transfer* **47**, 2971-2987.

[17] Hüttl, T. J. and Friedrich, R. 2001 Direct numerical simulation of turbulent flows in curved and helically coiled pipes. *Computers & Fluids* **30**, 591-605.

[18] Mees, P. A. J., Nandakumar, K. and Masliyah, J. H. 1996 Secondary instability of flow in a curved duct of square cross section. *J. Fluid. Mech.* **323**, 387-409.

[19] Fenstermacher, P. R., Swinney, H. L. and Gollub, J. P. 1979 Dynamic instability and the transition to chaotic Taylor vortex flow. *J. Fluid Mech.* **94,** 103-128.

[20] Collins, W. M. and Dennis, S. C. R. 1975 The steady motion of a viscous fluid in a curved tube. *Q.J. Mech. Appl. Math.* **28**, 133-156.

[21] Avila, M., Meseguer, A. and Marques, F. 2006 Double Hopf bifurcation in corotating spiral Poiseuille flow. *Phys. Fluids* **18**, 064101.